Mobile Vehicle-to-Vehicle Narrow-Band Channel Measurement and Characterization of the 5.9 GHz Dedicated Short Range Communication (DSRC) Frequency Band

Lin Cheng, *Student Member, IEEE,* Benjamin E. Henty, *Member, IEEE,* Daniel D. Stancil, *Fellow, IEEE,* Fan Bai, *Member, IEEE,* and Priyantha Mudalige, *Member, IEEE*

Abstract— This study presents narrow-band measurements of the mobile vehicle-to-vehicle propagation channel at 5.9 GHz, under realistic suburban driving conditions in Pittsburgh, Pennsylvania. Our system includes Differential Global Positioning system (DGPS) receivers, thereby enabling dynamic measurements of how large-scale path loss, Doppler spectrum, and coherence time depend on vehicle location and separation. A Nakagami distribution is used for describing the fading statistics. The Speed-Separation diagram is introduced as a new tool for analyzing and understanding the vehicle-to-vehicle propagation environment. We show that this diagram can be used to model and predict channel Doppler spread and coherence time using vehicle speed and separation.

Index Terms— Communication system, modeling, statistics, land vehicle, land mobile radio propagation factors.

I. INTRODUCTION

KEY goals of the design of highway and transportation systems are to reduce the occurrence of accidents and alleviate congestion. Tools such as vehicle sensors, speed radars, traffic cameras and other state-of-the-art technologies are frequently deployed to combat these problems. In 1999, the Federal Communications Commission (FCC) allocated 75 MHz of licensed spectrum, from 5.85 to 5.925 GHz, as part of the Intelligent Transportation System (ITS) to use for Dedicated Short Range Communications (DSRC)[1] in the United States. Since then, significant effort from the automotive industry has been focused on developing various kinds of new applications using DSRC technology to exchange information among vehicles, such as safety messages, traffic condition messages or rich media content [1]–[3].

[1]The IEEE 802.11p standard (or, DSRC) is a variant of the IEEE 802.11a standard. While keeping the key design and specification almost the same as IEEE 802.11a, a number of parameters in the IEEE 802.11p physical-layer specification have been changed to adapt to outdoor automotive environments. For example, IEEE 802.11p operates in a different frequency band near 5.9GHz. Also, the channel bandwidth of 802.11p is about 10 MHz compared to 20 MHz in 802.11a. However, the suitability of DSRC technology for automotive environments is still under technical evaluation.

Under development by the IEEE 802.11p standard committee, DSRC technology is targeted for nation wide deployment for different applications ranging from safety alert, collision avoidance, and congestion prediction, to social networks and passenger infotainment. While IEEE 802.11p based DSRC technology is promising for enabling wireless communication between vehicles, the detailed behavior of DSRC technology under various vehicle-to-vehicle (V2V) environments still remains an open question for both industry and the research community. Reliable knowledge of the propagation channel serves as the enabling foundation for robust, efficient, and practical design and testing of V2V communication systems. Thorough channel knowledge helps to understand a range of impairments such as attenuation, multi-path fading, and the time variations in the channel. In the V2V scenario, these impairments are correlated with mobility parameters such as speed, separation distance, driver behavior, etc. An understanding of these impairments is essential for the design of V2V communication systems that have optimal or near-optimal performance.

Theoretical models for the V2V channel have been discussed by a number of authors [4]–[10]. However, real driving environments do not always adequately satisfy the assumptions made in these models, such as the isotropic location of scattering sources around the mobile. Our work is complimentary to these results, because the empirical data collected in our study can be used to further validate various types of theoretical channel models proposed in the literature.

Other works that are more empirical in nature have been conducted at frequencies outside the 5.9 GHz DSRC band targeted for nation-wide deployment in the United States. Although the principles of channel impairment are similar, scattering and obstruction by various objects in the environment can vary significantly with frequency. A study by Davis *et al.* [11] reported vehicle-to-vehicle RF propagation measurements in the 900 MHz band between parked cars in a roadway environment. Vehicle-to-vehicle measurements at 915 MHz in a mobile environment were reported by Punnoose *et al.* [12], and joint Doppler-delay power profile measurements at 2.4 GHz were reported by Acosta, *et al.* [13]. A number of authors have reported measurements in the 5.2-5.3 GHz band. Maurer *et al.* [14] conducted flat-fading narrow-band

measurements of inter-vehicle transmission at 5.2 GHz, and Zhao *et al.* [15], [16] reported measurements in the indoor low-mobility environment at 5.3 GHz. More recently, [17] presented measurements at 5.9 GHz for a chosen highway site.

Many of these empirical studies also included analysis of fading statistics. Maurer *et al.* [14] studied narrowband fading distributions for the mobile-to-mobile channel at 5.2 GHz. They computed cumulative distribution functions (CDF) of the received signal levels from measured data for the fast fading components. Comparisons were made via a least square algorithm to Nakagami, Gaussian, Ricean and Rayleigh distributions. Results demonstrated that the Ricean distribution yields the smallest error between the measured data and the analytical functions. However a K factor was not given. Davis et al. [11] also studied Ricean K factors for the vehicle-to-vehicle line-of-sight (LOS) scenario at 900 MHz mentioned above. This study suggested that the channel may not be strictly Ricean owing to strong reflections off of the roadway in addition to the LOS component.

Measures of the mobile-to-mobile Doppler spectrum have been reported by Maurer *et al.* [14], Acosta *et al.* [13] [17], and Zhao *et al.* [15], [16]. Maurer *et al.* conducted flat-fading narrow-band measurements of inter-vehicle transmission at 5.2 GHz. Tapped channel modeling for vehicle networks has been reported in [13] as well as in [17]. [13] reported a joint Doppler-delay power profile measurement at 2.4 GHz, while a method to develop a channel emulator model for a doubly selective V2V wireless channel at 5.9 GHz was presented in [17]. Zhao *et al.* [15], [16] reported Doppler spectra from IEEE 802.11 type devices in the indoor low-mobility environment at 5.3 GHz.

We believe additional measurements are needed to thoroughly characterize the mobile V2V environment at the designated 5.9 GHz frequency band. Moreover, knowledge about channel statistics as a function of location are surprisingly lacking in the open literature. There also exists a need to develop channel models for realistic driving environments, i.e., environments for which the driving behavior is determined by traffic and other external factors and cannot be controlled by the driver. Motivated by these facts, we have taken a measurement oriented approach to gain a better understanding of the V2V wireless channel.

Our system setup has several key features that combine and extend the strengths of those previously reported. We have combined the advantages of Ref. [17] by performing measurements at 5.9 GHz and of Ref. [13] by performing measurements in a mobile environment. Further we extend the work of both references by incorporating GPS receivers into our measurement platform to allow dynamic measurement of the DSRC channel while the vehicles are being driven in actual roadway conditions. The usage of GPS receivers allows us to more completely characterize the V2V channel by collecting channel statistics over a wide range of vehicle speeds, separations and locations. The GPS receivers also help us overcome the difficulties in properly synchronizing measurements performed while the two vehicles are in motion as we discuss in this paper. Lastly, using a digital signal generator as a transmitter and a vector signal analyzer as a

receiver allows significant flexibility, especially compared to measurements based on received signal strength obtained from off-the-shelf radios such as a DSRC/IEEE 802.11p prototype radio developed by the Denso Corporation [18].

This experimental system serves as the primary platform for our study of the V2V radio propagation channel. Here we report characterization of the V2V channel along multiple dimensions: signal strength versus distance, fading models, coherence time, and Doppler analysis. In addition, we have developed insight into the impact of speed and separation distance on channel statistics. We summarize the contributions of this paper as follows

1) We report a fully mobile, V2V channel characterization platform which has a large dynamic range, extensive flexibility in transmission frequency and modulation for narrowband and wideband measurements, and an accurate synchronization and position location system for recording channel performance with vehicle speed, separation and location.

2) Using two large data sets taken in suburban Pittsburgh, we present single-slope and dual-slope large-scale path loss models including log-normal fading.

3) We present an analysis of the observed fading statistics using the Nakagami distribution and find that the fading gradually transitions from near-Rician to Rayeigh as the vehicle separation increases. When the line-of-sight is intermittently lost at large distances, the fading can be more severe than Rayleigh.

4) We have analyzed the Doppler spread and coherence time and present their dependence on both velocity and vehicle separation. We confirm the theoretically predicted dependence on $\sqrt{(v_R^2 + v_T^2)/2}$ [9] from our experimental on-road study.

5) We introduce the Speed-Separation (S-S) diagram as a new tool for understanding and estimating Doppler spread and coherence time in the V2V environment. In particular, this new tool enables a convenient methodology to generate accurate small-scale fading using only a model of driving behavior, with or without actual measurements.

It is worth noting that our measurements do not address the effects of co-channel interference that would occur with a large number of vehicles equipped with DSRC radios. The expected dominant effect from vehicles in the general vicinity would be reduction in throughput resulting from the carrier sense multiple access (CSMA) protocol and packet collisions. In contrast, large numbers of distant co-channel interferers would be expected to increase the noise floor, since the interference would tend to have a Gaussian distribution through the Central Limit Theorem.

II. MEASUREMENT PLATFORM

A. Overview

To characterize a channel that is as dynamic as those found in realistic driving environments, empirical measurement campaigns are needed. Our early work (unpublished) on this subject was conducted using prototype DSRC radios made by Denso [18]. At that time, measurements were

performed for vehicles traveling with various mobilities and separations in different environments (e.g., highway, suburban, etc). Fading analysis was conducted by characterizing the measured Received Signal Strength Indicator (RSSI) value in different distance bins using a probability density function. However, this method has three major limitations. First, the recorded RSSI is not sufficient for understanding RF channel statistics like the delay spread and Doppler spectrum. Second, the prototype DSRC radio reports an RSSI value only if the corresponding packet is successfully received. For the Denso prototype DSRC radio, the receive power threshold is approximately -95 dBm. The absence of the dropped packets' RSSI values below -95 dBm introduces skew in the statistical channel characterization. The unknown nature of the channel makes prediction of these dropped packets' RSSI values even more difficult. Finally, spectral analysis of the DSRC channel from our measurements has shown that interfering signals are often present within the channel. At large distances when the signal power is weak, these interfering signals may make significant contributions to the power in the received channel. Since radios typically report the total analog power in the channel when a packet is received, the presence of this interference power artificially elevates the received signal level at large distances, adding additional skew to the data. The combined effects of the skew from dropped packets and interference can result in apparent path loss exponents significantly less than 2.

These observations have led us to develop an RF measurement system using a re-configurable digital signal generator (DSG) and a vector signal analyzer (VSA) [19]. This system is aimed at understanding the RF channel by capturing statistics such as the delay spread and Doppler spectrum. When used with narrowband signals, these precision instruments enable a large dynamic range, so that the skews from the noise floor can be significantly reduced. The likelihood of significant interference power in narrowband measurements is also reduced, and the ability to examine the channel spectrum enables measurements with interfering signals to be identified. Finally, the statistics derived from our RF measurement system can be used to partially correct the biased data from the prototype DSRC radio using estimation techniques.

B. System Architecture

The system architecture of the transmitter is depicted in Fig. 1(a). An Agilent E4433A Digital Signal Generator (DSG) is used for signal generation. It is capable of generating signals up to 4.0 GHz. To obtain a continuous wave (CW) signal at 5.9 GHz, a 2.95 GHz signal from the generator is frequency doubled using a mixer and the signal from the coherent carrier output of the DSG. The coherent carrier output is a fixed power signal at the same frequency as the carrier tone of the generated digital signal. This technique simply avoids the need for a second local oscillator. While this technique results in a total frequency drift double the inherent drift of the DSG, the drift is still quite low and is far better than the drift that would be added from an additional, inexpensive crystal oscillator. A low-pass filter (LPF) is used to remove undesired harmonics in the coherent carrier ouput. Another band-pass filter (BPF)
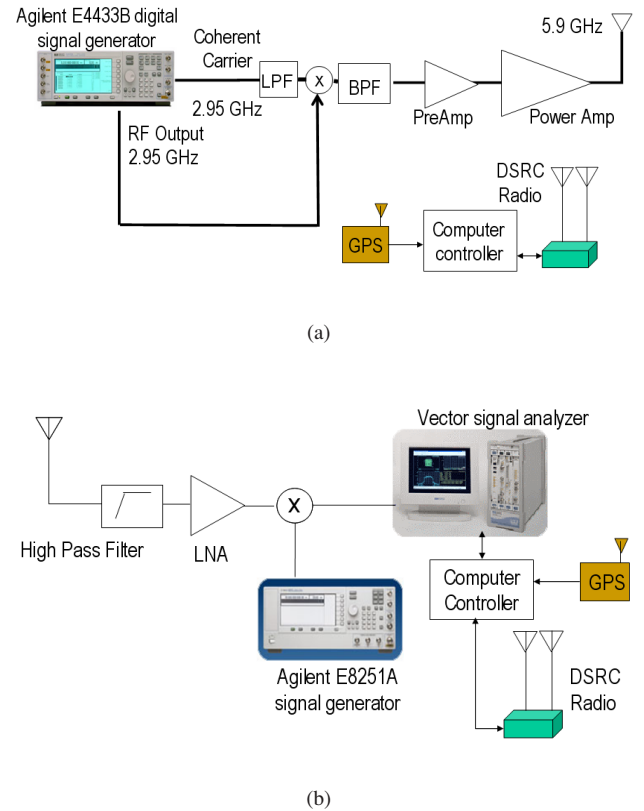

(a)

(b)

Fig. 1. System setup for the channel sounding measurements: (a) the setup on the transmitting vehicle, and (b) the setup on the receiving vehicle.

is used to ensure undesired mixer products are removed before transmission. Lastly, two stages of amplification are used to reach a power level of 19.5 dBm – a value comparable to expected DSRC transmit levels. The gains of the antennas used are about -4 dB in the forward and reverse directions. The antennas were mounted on the roofs of the vehicles, resulting in a height of 1.51 m for the transmit antenna and 1.93 m for the receive antenna.

Fig. 1(b) describes the system setup at the receiver side. A broadband, low noise amplifier with a noise figure of 1.4 dB is used to maximize the sensitivity of the receiver. To prevent a loss of gain due to out of band signals, a high-pass filter is used which provides a minimum of 40 dB of attenuation to all signals below 3.8 GHz and 1 dB of attenuation across the 5.9 GHz frequency band. A mixer is used to down-convert the received RF signal into the 0 to 40 MHz range that can be analyzed by the Agilent 89600 Vector Signal Analyzer (VSA). The VSA is set to measure a small range of frequencies around the CW tone to further improve the system dynamic range. The sensitivity of our narrow-band system referred to the receiver antenna is -148 dBm for a 4 kHz system bandwidth. The difference between this and the -95 dBm sensitivity of the prototype DSRC radios is primarily due to the difference in bandwidth and the lower noise figure of the experimental receiver system. Automation software is used to record a data capture of the signal at intervals between 1 and 3 seconds. We refer to each of these captures as a VSA measurement sweep. An Agilent 8251A precision RF signal generator is

used to provide a LO signal to the mixer at the receive side. Oscillator drift between the VSA and the Agilent E8251A signal generator is prevented by connecting the instruments' 10 MHz reference clocks.

Measurements of the the relative carrier drift between the transmitter and receiver systems was found to be about 3 Hz per minute at 5.9 GHz. This is less than one part per billion per minute and less than one part per million per day. In all cases, the drift over a measurement sweep is negligible.

To obtain position information, both vehicles are equipped with a CSI Wireless Differential GPS (DGPS) receiver and a Linux laptop computer that logs GPS data. The accuracy of the WAAS (Wide Area Augmentation System) based DGPS is on the order of 1 meter.

A fundamental issue with V2V measurements is the necessity of synchronizing the data collected in two separate, mobile vehicles. We overcome this difficulty through the calculation of an accurate timebase in both vehicles using multiple time stamps. The local time reported by the GPS and the computer's system time are both recorded during the measurements. Since our GPS measurements are recorded at a rate of 5 Hertz, we need to ensure the time base in both vehicles is identical to within 100 milliseconds or better. Unfortunately, clock drift in laptops is on the order of 1 second or more per day. This may be too high for reliable synchronization, especially when used outdoors over multi-hour measurements, so the computer system times should not be relied upon for accurate time synchronization. GPS time stamps can also be unreliable. GPS time stamps can show large differences from local time on a moment by moment basis, but over longer time scales such as the length of a measurement run, should show a very small average error. The accuracies of the laptop time stamps and the GPS time stamps are, however, complementary and we have combined these time stamps into a single precise timebase for each vehicle. This method is quite advantageous because the laptop time stamps are accurate over the short term, but may have large mean errors and some drift over the long term while GPS time is accurate over the long term but may have significant errors over the short term. Thus, after combining the time stamps in each vehicle, we can be certain that the timebases for the data collected by each vehicle are sufficiently accurate for synchronizing the data logs of the two vehicles.

We have also used NTP (Network Time Protocol) [20] to ensure the clock of the VSA computer is synchronized with the linux laptop used for recording position information. In our system, we configure an NTP server on the linux laptop in the receiver vehicle and configure the VSA computer as an NTP client. We set up a local area ethernet network within the vehicle. The NTP server can use its own clock as the reference clock and the VSA computer synchronizes its system clock to the linux laptop.

We initially used an alternative method in some of our early test measurements for clock synchronization. This method is similar to that used by NTP for synchronizing computer clocks connected to the same IP (Internet Protocol) network. The method uses the transmission of time information between vehicles to synchronize the data clocks. It was not used for the data presented herein, but can be quite useful when GPS time is unavailable and so is presented in the Appendix.

Aside from the wireless signals to be measured by the DSG/VSA pair, we enable communication between the two vehicles using two prototype DSRC radios. These radios support IP (Internet Protocol) communications and extend the functionality of our measurement system by providing a means for exchanging time-stamp and location information between vehicles. Additionally, the performance of these radios can be correlated with the simultaneous measurements of the channel properties. The prototype DSRC radios operate at a channel different from those being measured with the DSG and VSA to avoid interference. A User Datagram Protocol (UDP) packet containing time-stamp, GPS information (e.g. latitude, longitude, position, speed, heading, etc.) and a unique packet sequence number is sent from each vehicle five times per second. All of the transmitted data packets are also stored on the local computer along with the recorded GPS data.

C. Flexibility

As previously mentioned, the system architecture described above is not limited to narrow-band, CW signals. Wide-band measurements are required to measure the coherence bandwidth and delay spread properties of a channel. These properties are critical to understanding the performance of a radio link in a rich multipath environment. The flexibility of the programmable DSG allows wide-band measurements with different modulation schemes, e.g., wide-band OFDM or DSSS signals. The system architecture at the receiver side remains unchanged. The VSA is simply programmed with the appropriate bandwidth, up to 40 MHz, for the transmitted signal. In addition, the VSA is capable of demodulating and decoding the received signals. This allows us to receive and analyze an arbitrary test signal.

Given a modulation scheme, the VSA at the receiver can be programmed to record the signal constellation, the OFDM spectra, the Error Vector Magnitude (EVM), the actual bits received, the equalizer's response and the received waveform. This provides the building blocks for measuring the properties of modulated signals, such as Bit Error Rate (BER) and delay spread. We leave the topic of wide band measurements for another study.

III. SIGNAL AND DATA PROCESSING

Both synchronization and data processing are performed as post-processing steps. After synchronizing the data logfiles of the two vehicles, GPS speed and location information is associated with VSA measurements. Since the GPS update rate (200 ms per update) is different from the VSA sweep recording rate (1 sweep every 1-3 s), we start with each VSA sweep entry and look for the GPS data having the closest time stamp. Special care is taken to ensure that measurement data with invalid GPS information due to a GPS outage are eliminated.

Channel parameters such as pathloss and coherence time are computed from VSA time-domain recordings. For signal strength and Doppler spread studies, the time-domain recordings are transformed to the frequency domain using a discrete Fourier Transform (DFT). When two vehicles are moving in opposite directions with a relative speed of 120 mph, the
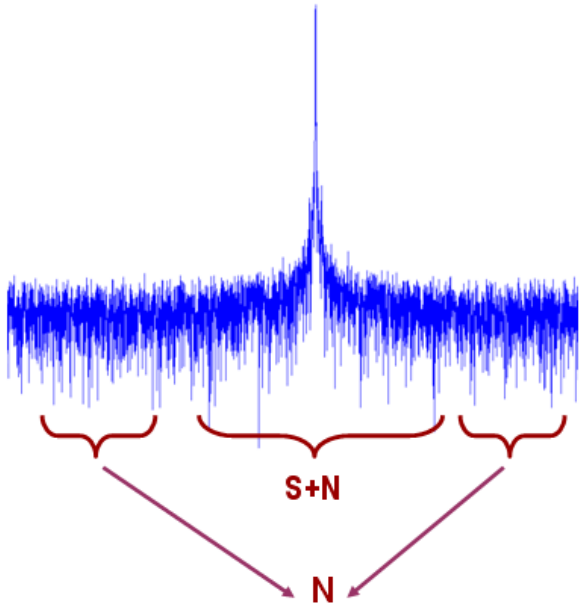
Fig. 2. Computation of the signal and noise strengths, where S is signal and N is noise.

TABLE I
DATA SET DESCRIPTIONS

Parameter	Data Set 1	Data Set 2
Sweep duration (s)	1.5	0.2
Number of points in sweep	7580	1024
Interval between sweeps (s)	0.8-1.8	1
Number of sweeps	889	5567
VSA bandwidth (kHz)	4	4
Route	Fig. 3(a)	Fig. 3(b)

The measurement parameters for the data sets are given in Table. I, and the routes are shown in Fig. 3(a) and Fig. 3(b). These routes consist primarily of 2-lane suburban streets, and the experimental vehicles did not pass each other during the data runs. The width of these 2-lane suburban streets in Pittsburgh is on the order of 8 to 10 meters, with houses and buildings set back 10-12 meters from the curb. It is worth noting that in other parts of the world, e.g., Japan and Europe, there are suburban streets that are narrower than those seen in our study. This could produce different observations with respect to the channel statistics. From the confidence intervals estimated for our measurements (shown in subsequent data plots) we believe these data sets are large enough to draw statistically meaningful conclusions.

Doppler shift will be about 1 kHz. In view of this, we chose a 4 kHz bandwidth to ensure the most likely Doppler frequency spread would be captured while still leaving room for carrier drift and allowing for an adequate sampling of the channel noise level.

Making use of ergodicity, the signal strength is computed in the frequency domain instead of the time domain. This more easily enables us to distinguish between signal and noise power. We first identify a frequency range that captures all of the signal power. Integrating the power spectrum profiles over this range gives the signal plus noise power, which is shown as $S + N$ in Fig. 2. Integrating the power spectrum profiles over remaining portions of the spectrum with the same number of frequency bins gives an independent measure of the noise power, which is shown as N in Fig. 2. Both integrations are conducted for each individual sweep. The signal strength S in each sweep is then obtained by the subtraction of these two integrals.

Location statistics such as distance and velocity are computed from raw GPS recordings. The distance between vehicles is computed by the Haversine formula [21], [22], using the latitude and longitude coordinates of the two vehicles, where the radius of the earth is optimized for locations approximately 39 degrees from the equator. The velocity is computed from the heading and speed estimates provided by the DGPS receiver.

IV. EXPERIMENTAL DATA SET DESCRIPTIONS

We conducted two sets of narrow-band Continuous Wave (CW) experiments on June 7th, 2006 (Data Set 1) and on Feb 7th, 2007 (Data Set 2) in suburban driving environments near Carnegie Mellon University in Pittsburgh, PA. Two vehicles, a transmitter and receiver, are equipped with our measurement system. Both vehicles were driven at each driver's prerogative, to preserve normal driving conditions. As a result, the distance between vehicles varied from 2 to 600 meters.

V. LARGE SCALE CHANNEL MODELING AND FADING ANALYSIS

Accurate large-scale channel models play a vital role in the design, evaluation, and validation of network protocols, which are critical to the deployment of large-scale systems. While prototype DSRC devices are currently available, there currently is no widely-accepted channel model for V2V network simulations. With this view in mind, we discuss important concepts like path loss, shadowing, and fading statistics. The objective of this work is to provide hierarchical models ranging from simple to complex to address the needs of various types of system modeling and simulation. In addition, we identify the limitations of modeling based on RSSI values reported by DSRC radios, and show that our system effectively addresses these limitations.

A. Path Loss Models

To obtain large-scale path loss models, we compute both the Received Signal Strength (RSS) and the distance between the two vehicles. First, we present the path loss measurements via a widely used log-normal model. The generic form of this model is given as

$$P(d) = P(d_0) + 10\gamma \log\left(\frac{d}{d_0}\right) + X_\sigma, \qquad (1)$$

where $P(d)$ is received signal strength at distance d and $P(d_0)$ is its counterpart at reference distance d_0. Linear regression is used to estimate the path loss exponent γ and random variable X_σ. Here X_σ is a zero-mean, normally distributed random variable with standard deviation σ. The results of linear regression analysis of the two data sets are shown in Table II, and the resulting curves shown as the solid lines in

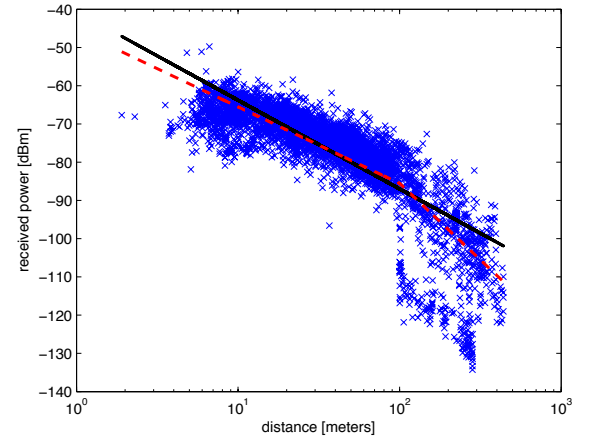(a) Data set 1
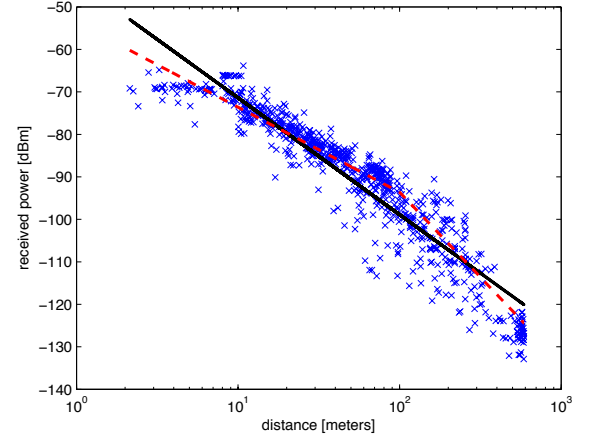
(b) Data set 2

Fig. 3.   Routes taken for (a) Data set 1, and (b) Data set 2. Each data set contains multiple laps around the respective route.

(a) Data set 1

(b) Data set 2

Fig. 4.   Pathloss measurements and approximate large-scale models. (a) Data set 1. Black line: single-slope model with γ=2.75 and σ=5.5dB. Red dashed line: dual-slope model with γ_1=2.1, σ_1=2.6dB;γ_2=3.8, σ_2=4.4dB;and d_c=100 m. (b) Data set 2. Black line: single-slope model with γ=2.32 and σ=7.1dB. Red dashed line: dual-slope model with γ_1=2, σ_1=5.6dB;γ_2=4, σ_2=8.1dB;and d_c=100 m.

Fig. 4(a) and 4(b). The pathloss exponent ranged from 2.32-2.75, and the standard deviation ranged from 5.5-7.1 dB.

However, in practice, a dual-slope piecewise-linear model is able to represent the measurements more accurately. We characterize this piecewise model by a path loss exponent γ_1 and a standard deviation σ_1 within a critical distance d_c. Beyond this critical distance, the signal strength falls off with another path loss exponent γ_2 with a standard deviation σ_2 . The formula of this model is given as

$$
P(d) = \begin{cases} P(d_0) - 10\gamma_1 \log_{10}\left(\frac{d}{d_0}\right) + X_{\sigma_1} & \text{if } d_0 \le d \le d_c \\ P(d_0) - 10\gamma_1 \log_{10}\left(\frac{d_c}{d_0}\right) - & \text{if } d > d_c \\ \quad 10\gamma_2 \log_{10}\left(\frac{d}{d_c}\right) + X_{\sigma_2} & \end{cases}
$$

(2)

In the conventional flat earth model, d_c is taken to be the distance where the first Fresnel zone touches the ground and is referred to as the Fresnel distance. The distance for the first

Fresnel zone can be calculated as $d_F = \frac{4h_T h_R}{\lambda}$, where h_T and h_R are antenna heights of the transmitter and the receiver respectively, and λ is the wavelength of the electromagnetic wave at 5.9 GHz. The heights of the antennas on our vehicles were h_T=1.51m and h_R=1.93m, giving a Fresnel distance of 225 m. However, we allowed d_c to be an adjustable parameter in our data analysis.

The results of a piecewise linear fit of this model to the data sets are also given in Table II and depicted as dashed lines in Fig. 4(a) and Fig. 4(b). As indicated by the standard deviations, the dual-slope models generally fit the data more accurately. We found that placing the breakpoint at the theoretical Fresnel distance of 225 m results in larger standard deviation values than those obtained with a critical distance of 100 m, implying a poorer fit. A critical distance

TABLE II
LARGE-SCALE PATH LOSS MODEL PARAMETERS

Parameter	Data Set 1	Data Set 2
Single slope γ	2.75	2.32
Single slope σ (dB)	5.5	7.1
Dual slope γ_1	2.1	2
Dual slope σ_1 (dB)	2.6	5.6
dual slope γ_2	3.8	4
Dual slope σ_2 (dB)	4.4	8.4
Critical distance $d_c(m)$	100	100

less than the Fresnel distance has also been reported by [23], and may be caused by the presence of vehicles, pedestrians and other objects on the road creating reflections from points higher than the ground.

Note in dataset two, we observe a second band of data points below the main band at large distances. GPS traces show that this band generally resulted when the two vehicles were traveling on parallel streets, or were separated around a corner. In this case the houses and buildings between the vehicles increased the attenuation and intermittently obstructed the line-of-sight. This observation suggests the desirability of a multi-state model, with different states being applicable when a line-of-sight does and does not exist between the vehicles. This will be a topic of future work. The points in the lower band resulting from parallel streets were excluded from the linear regressions described above, but points occurring when the vehicles made turns were retained.

In classical propagation models, the log-normal model is a statistical description of random variations in signal strength that are observed over distances large compared to a wavelength and are the result of scattering by and transmission through multiple objects and obstructions. This large-scale fading, referred to as shadowing, is distinct from the small-scale fading that occurs on the scale of a wavelength and results from interference between multipath components. The total fading observed is generally a combination of these two effects. Due to the small distance scales and dominance of the line-of-sight component in V2V channels, it is likely that the fading is dominated by small-scale fading with very little shadowing. In this case X_σ is actually not a Gaussian random variable, but rather has statistics determined by the small-scale fading. (If the fading is Rician with a large K factor, a Gaussian distribution is a good approximation, however.) Thus our use of the form of the classical log-normal model in Eqs.1 and 2 should really be seen as an approximate way of describing the observed scatter about the large-scale trend, rather than actually arising from the classical shadowing phenomenon.

B. Comparison with Prototype DSRC Radio

Having described the large-scale path loss measured with the narrowband instrument system, we now compare our results with those obtained from the prototype DSRC radios [18]. Fig. 5 shows the path loss plot from the same suburban environment in data set two using the prototype DSRC radio.
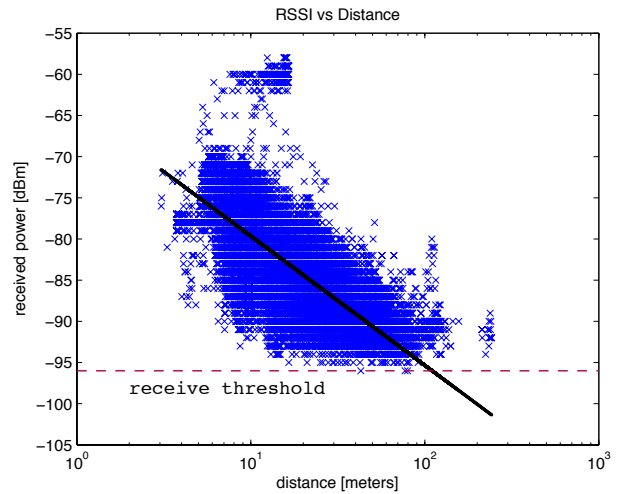

Fig. 5. Pathloss measurements obtained from prototype DSRC radio RSSI values. No measurements are obtained for packets below the receive threshold. For the linear regression, γ=1.57 and σ=4.2dB.

The linear regression shown gives γ=1.57 and σ=4.2 dB. The loss of packets with RSSI below the threshold indicated by the dashed line is apparent. It can also be seen how this loss of data contributes to a skew towards a smaller slope than would be obtained if, for example, the slope of the top edge of the band of data were estimated. Although not apparent from Fig. 5, we have also discovered that interference signals often contribute to the total received power, artificially elevating the RSSI at larger distances. Use of the narrowband system reduces both the sensitivity and interference problems to negligible levels over the range of signals and distances encountered in our data sets.

C. Fading Analysis

In the discussion above, we commented that the random variable X_σ used in the model may not be Gaussian if it is dominated by small-scale fading rather than shadowing. Consequently, a refinement to the coarse model described in the previous sections is to determine what the empirical distribution of X_σ actually is, and interpret this in terms of small-scale fading models such as Rician and Rayleigh fading.

Nakagami distributions, Rician distributions, and Rayleigh distributions are widely used to model scattered signals that reach a receiver by multipath. Depending on the density of the scatterers, the total received signal exhibits different fading characteristics. Rician distributions model fading with a single stronger line-of-sight in the presence of scatterers, while Rayleigh distributions are used to model dense scatterers when no line-of-sight is present. The Nakagami distribution is a more general model that can represent Rician, Rayleigh, or fading that is more severe than Rayleigh, depending on model parameters, and thus is capable of describing a wide range of fading situations. Given the varied driving environments, we use the Nakagami distribution in the following analysis.

The procedure for the Nakagami analysis was as follows. The raw signal strength (linear amplitude) versus separation data was smoothed with a sliding average to identify the large-scale component of the variations. This large-scale component

TABLE III

DATA SET 1: ESTIMATED VALUES OF THE SHAPE PARAMETER μ AND D STATISTIC ACROSS THE DISTANCE BINS FROM CW MEASUREMENTS USING OUR CHANNEL MEASUREMENTS SYSTEM. ALL DISTRIBUTIONS ARE NORMALIZED TO $\omega = 1$.

Distance bin (in meter)	μ	D statistic
From 0.0 to 5.5	4.07	0.20
From 5.5 to 13.9	2.44	0.13
From 13.9 to 35.5	3.08	0.07
From 35.5 to 90.5	1.52	0.10
From 90.5 to 230.7	0.74	0.10
From 230.7 to 588.0	0.84	0.13

TABLE IV

DATA SET 2: ESTIMATED VALUES OF THE SHAPE PARAMETER μ AND D STATISTIC ACROSS THE DISTANCE BINS FROM CW MEASUREMENTS USING OUR CHANNEL MEASUREMENTS SYSTEM. ALL DISTRIBUTIONS ARE NORMALIZED TO $\omega = 1$.

Distance bin (in meter)	μ	D statistic
From 0.0 to 4.7	3.01	0.19
From 4.7 to 11.7	1.18	0.06
From 11.7 to 28.9	1.94	0.03
From 28.9 to 71.6	1.86	0.04
From 71.6 to 177.3	0.45	0.14
From 177.3 to 439.0	0.32	0.13

was then used to normalize the the raw data so that the average of the amplitude squared was unity, independent of distance. Next we divided the separation distance into several bins, with the amplitude values within each distance bin forming empirical distributions to be fit with a Nakagami distribution. The Nakagami distribution is given by (μ, ω)

$$f(x; \mu, \omega) = \frac{2\mu^\mu x^{2\mu-1}}{\omega^\mu \Gamma(\mu)} e^{\frac{-\mu x^2}{\omega}}, \qquad (3)$$

where μ is a shape parameter, and $\omega = E[x^2]$ is an estimate of the average power in the fading envelope. When $\mu = 1$ the Nakagami distribution describes a Rayleigh distribution, while for $\mu > 1$ the distribution is Rician. For the empirical distribution in each distance bin, we performed maximum likelihood estimation (using the log-likelihood function) to optimize the parameter μ for the Nakagami distribution.

Finally, we applied the Kolmogorov-Smirnov test (K-S test) to evaluate the fit to the empirical distribution. We used the K-S test because this test statistic does not depend on the underlying cumulative distribution function being tested. In addition, as opposed to tests that depend on an adequate sample size to obtain valid approximations (e.g., the chi-square goodness-of-fit), the K-S test is a rigorous test that does not have dependency on binning [24].

We denote the hypothesized cumulative distribution as $F(x) = P(X_1 \leq x)$. We define the empirical distribution function $F_n(x)$ for n observations y_i by

$$F_n(x) = \frac{1}{n} \sum_{i=1}^{n} \begin{cases} 1 & \text{if } y_i \leq x \\ 0 & \text{otherwise} \end{cases} \qquad (4)$$

which counts the proportion of the empirical sample points below signal strength x. The results of the K-S test rely on the biggest discrepancy value between the empirical cumulative distribution and the hypothesized cumulative distribution, which is defined as the D statistic

$$D = \max_x ||F(x) - F_n(x)||. \qquad (5)$$

For a rigorous test of the Nakagami hypothesis, the D value should be compared with a threshold value. However, we simply use the D value to assess how well the Nakagami distribution fits the data.

Fig. 6(a) and Fig. 6(b) show both the empirical cumulative distribution and hypothesized cumulative distribution for several distance bins for each data set. The distance bins

are divided based on the logarithm of the total range of the distance data points. The dashed lines represent the empirical CDF while the continuous lines represent the hypothesized CDF. The agreement between the experimental and hypothesized CDFs can be seen to be good. Table III and Table IV summarize the key parameters in all the distance bins in each data set.

In Data Set 1 we observe that the fading follows a Rician distribution where μ values are larger than 1 at short distances, tending toward Rayleigh fading ($\mu = 1$) at larger distances. A similar trend is also found for Data Set 2. In both data sets the μ values at large distances indicate fading more severe than Rayleigh fading ($\mu < 1$) (i.e., pre-Rayleigh fading). We believe the reason for this is intermittent loss of line-of-sight at large distances, e.g., when vehicles are separated around corners. We expect the fading analysis conducted above not only to be useful for channel characterization in V2V scenarios, but also to serve as a meaningful parameter estimate on the density of the scatterers and the level of the attenuation present [25].

The fading analysis can be combined with the large scale path loss model by first using the path loss model to calculate the average expected power, setting this average power to the ω parameter in the Nakagami distribution, and selecting the μ parameter appropriate for the distance according to Table III and Table IV. The Nakagami distribution with these parameters may then be used to generate random values of the received signal amplitude at the distance selected.

VI. THE SPEED-SEPARATION DIAGRAM

As indicated above, the GPS position and velocity of each vehicle is logged for each VSA measurement sweep. The separation between the vehicles is readily obtained from these GPS logs. The velocities of the vehicles determine the Doppler spread, and according to models with isotropic scatterers, the Doppler spread is given by [4], [9]

$$f_D = \left(\frac{1}{\lambda}\right) \sqrt{\frac{v_R^2 + v_T^2}{2}} = \left(\frac{1}{\lambda\sqrt{2}}\right) v_{eff}, \qquad (6)$$
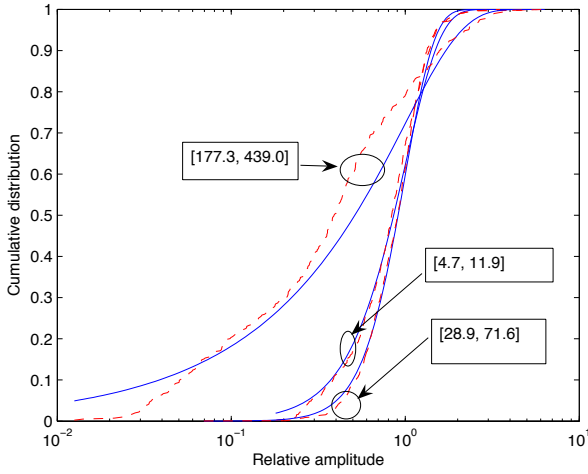
where v_R and v_T are the speeds (magnitudes of the velocities) of the receiving and transmitting vehicles, respectively. We have defined an effective speed as $v_{eff} = \sqrt{v_R^2 + v_T^2}$. Scatter plots of v_{eff} versus separation are shown in Fig. 7. We will refer to these plots as Speed-Separation (S-S) diagrams. An
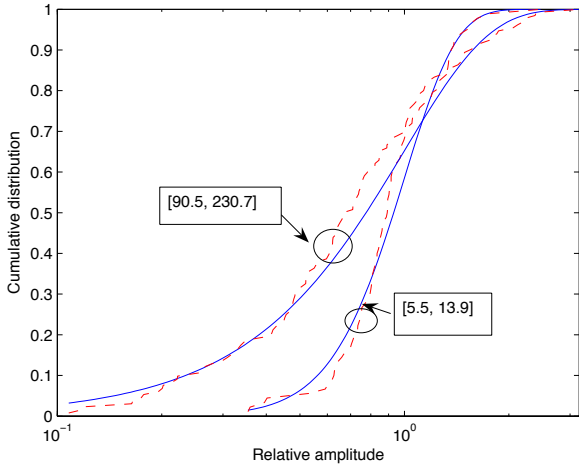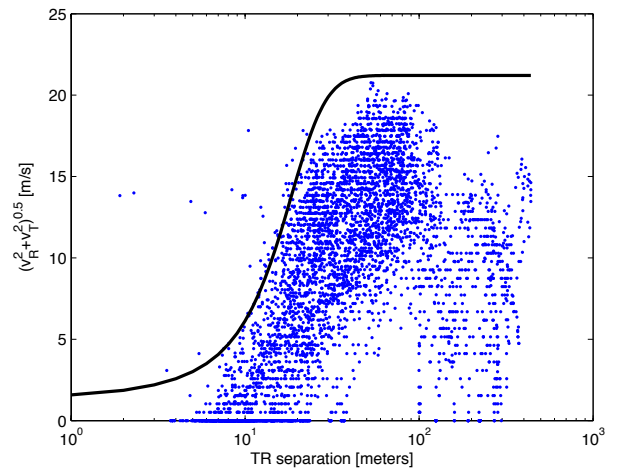
(a) Data set 1
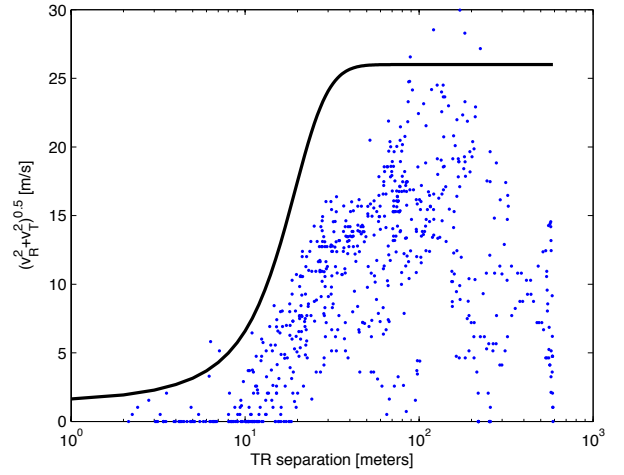
(b) Data set 2

Fig. 6. Comparisons between selected experimental cumulative distribution functions and theoretical fits using the Nakagami distribution. (a) Data set 1, (b) Data set 2. The curves are labeled with the limits of the distance bins given in meters.

(a) Data set 1

(b) Data set 2

Fig. 7. Scatter plots of $\sqrt{(v_R^2 + v_T^2)}$ versus vehicle separation for each measurement. (a) Data set 1, (b) Data set 2. The solid lines show the bounds given by the phenomenological model adjusted to fit the observed driving behavior [26].

interesting observation is that the data from the two different experiments exhibit similar patterns, which we interpret in terms of driver behavior. Beyond a minimum separation of about 5 m, the speed increases with separation up to the speed limit. The correlation of speed with distance reflects the natural tendency of drivers to allow greater separation as the speed increases. Both data sets also show a decrease in speed beyond about 100 m. The driving factors giving rise to this driving behavior are presently under study, but one of the reasons may be due to a desire of drivers to stay together.

This underlying correlation between separation and speed must be taken into account when analyzing the data for dependence on speed and separation. This led us to develop a phenomenological model to describe the relationship between the separation d and the maximum effective speed $v_{eff,max}(d) = \max(\sqrt{(v_R^2(d) + v_T^2(d))})$ observed at that separation [26]

$$v_{eff,max}(d) = \frac{v_{limit}}{1 + e^{-\alpha(d-d_0)}}. \qquad (7)$$

Here v_{limit} is the maximum value of v_{eff} observed during a data run, and α, d_0 are adjustable parameters. In our analysis, we tune α and d_0 to control the steepness and position of the function to obtain the best match with the top edge of the actual measured data (here $\alpha = 0.18m^{-1}$, $d_0 = 16m$ are found to fit well). As shown in Fig. 7, this phenomenological model bounds the points in the S-S diagram with reasonable accuracy for both data sets.

We will return to the properties of the S-S diagram in subsequent sections to show how it can be used to understand and predict key properties of the channel.

VII. DOPPLER ANALYSIS

We start this section with the underlying physics of Doppler spread. If signals from multiple paths are received by a moving vehicle, the observed frequency of each signal will be Doppler shifted depending on the component of the vehicle velocity along the direction of arrival of the path. All of the received signals are summed together at the receiver resulting in a broadened spectrum compared to the transmitted signal. This phenomenon is referred to as Doppler spread. In addition to path loss over large distances, the receive antenna will also experience fluctuations in signal level that vary significantly over distances on the order of one to tens of wavelengths, which is denoted as small-scale fading. The fluctuation is caused by both the multi-path propagation and the Doppler spread. Notice we use the Doppler spread instead of a simple shift of the frequency of the signal with relative velocity but due to this Doppler spread. In other words, Doppler spread made an impact in small-scale fading as the received signals of different frequencies go in and out of phase with one another.

The Doppler spread can be characterized quantitatively using spectral estimation. The nth order central moment of a spectrum, M_n, is described by

$$M_n = \frac{\sum (f_i - f_0)^n S(f_i)}{\sum S(f_i)} \qquad (8)$$

where f_i is the ith frequency in the spectrum sample, f_0 is the first order moment of the spectrum

$$f_0 \equiv \frac{\sum f_i S(f_i)}{\sum S(f_i)}, \qquad (9)$$

and $S(f_i)$ is the magnitude of the Doppler spectrum at frequency f_i. In the above equations, the denominator acts to normalize the spectrum to unit area.

The second order central moment, M_2, is used as a spectral width estimator for Doppler spread. Higher order moments can further quantify the spectrum details [27] [28]. For example, M_3 could be used to quantify the degree of asymmetry, or the skewness in the spectrum. The sign of M_3 also implies whether the skewness is to the left or right. M_4 can reflect the degree of flatness near its center, or quantify the departure from the nicely shaped spectrum when two vehicles are parked stationary to each other. Since the second order moment is enough to capture the width of the Doppler spectrum, we use it as the quantitative indicator of Doppler spread in our study. In terms of the second order moment, the experimental Doppler spread is given by

$$B_{D,E} = \sqrt{M_2}. \qquad (10)$$

The measured Doppler spread values versus effective speed are shown in Fig. 8 for both data sets. The contour plot in Fig. 8(a) shows the general trend of circular contours as expected from a dependence on speed of the form $\sqrt{v_R^2(d) + v_T^2(d)}$. Fig. 8(b) shows the dependence of Doppler spread on the effective velocity. The error bars in the plot represent the 95% confidence intervals. Also shown is the theoretical curve given by Eq. 6. A linear regression to Data Set 2 is also plotted as a solid line. The data confirms the predicted linear dependence, though the slope is smaller,

and an offset is apparent at zero speed. We believe the smaller slope is the result of fewer, non-isotropically oriented scattering objects than assumed in the models, resulting in smaller Doppler spreads on average than predicted. The offset is likely due to the fact that there is motion in the environment even when both vehicles are stationary. Fig. 8(c) shows the Doppler spread from Data Set 1. The smaller data set results in larger confidence intervals, but the trend is consistent with that of Data Set 2 shown in Fig. 8(b). The empirical dependence of Doppler spread on effective velocity is found to be

$$B_D = \left(\frac{0.428}{\lambda\sqrt{2}} \right) v_{eff} + 11.5. \qquad (11)$$

The dependence of Doppler spread on relative velocity is shown in Fig. 9. In contrast to the dependence on effective speed indicated in Fig. 8, there does not appear to be a strong dependence of the Doppler spread on relative velocity, at least to lowest order.

It is interesting to note that the average Doppler spread values shown in Fig. 9 are in good agreement with the value of 85.6 Hz observed at 5.2 GHz in urban and suburban environments [14]. This suggests that our results may also be applicable to frequencies differing by at least up to 10-12%.

Fig. 10 shows the computed value of Doppler spread versus vehicle separation using Eq. 10. For these calculations, the Doppler spread for each sweep was calculated, then the spreads in each distance bin were averaged. As shown in the figure, the averaged Doppler spread generally increases as separation increases in our V2V environments. The error bars in the plot represent the 95% confidence intervals.

It is interesting to compare this result with a similar study in [13] that compared Doppler spectra in different delay bins of the power-delay profile. As shown in Fig. 6 of [13], when the delay increases, the spectra evolve from narrow to wide and from smooth to varied, implying a corresponding increase in Doppler spread. The short delay available in the early delay bins limits the number of reflections that appear in the received signal. On the other hand, in larger delay bins, multipath components begin to dominate and widen the Doppler spectrum. In our measurements, we also expect that as the distance increases, the number of scatterers contributing to the received signal increases. However, we also find that the spreading is the result of the tendency for the vehicle speeds to be larger at larger distances. This appears to be the dominant effect for our data, as we now discuss.

We established in Fig. 8 that the Doppler spread is proportional to the effective speed $v_{eff}(d) = \sqrt{v_R^2(d) + v_T^2(d)}$. Using this observation, an approximation to the Doppler spread for a given distance bin can be constructed using the S-S diagram in Fig. 7. Consider the points that lie in a particular range of distances in either Fig. 7(a) or (b). Since the Doppler spread is proportional to the effective speed, each point in the bin contributes to a particular value of spread. By averaging all of the resulting Doppler spreads (or equivalently averaging the effective speeds) in a particular distance bin, an estimate of the Doppler spread for that distance is obtained using Eq. 11. The Doppler spread versus distance curves calculated in this way for the two data sets are shown as the curves marked with "*" in Fig. 10. The agreement with the values
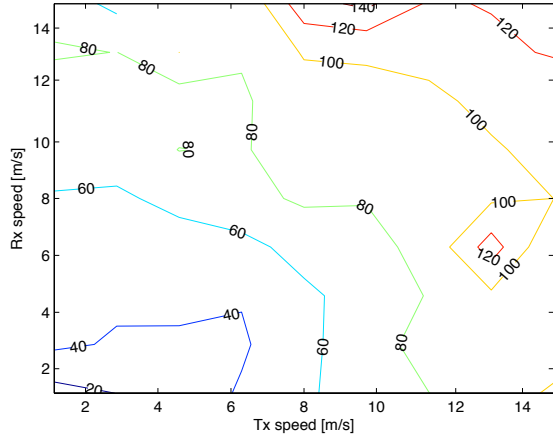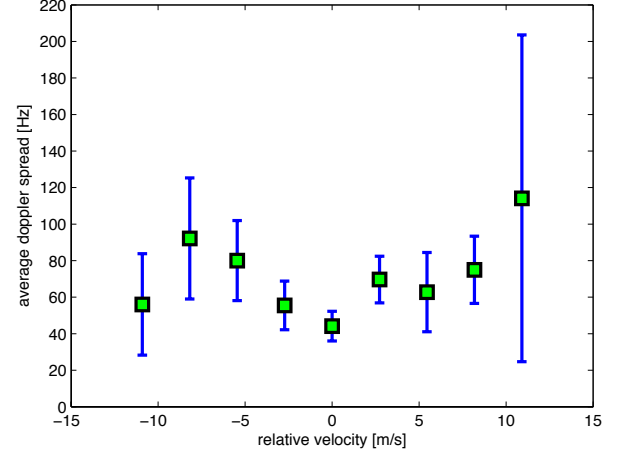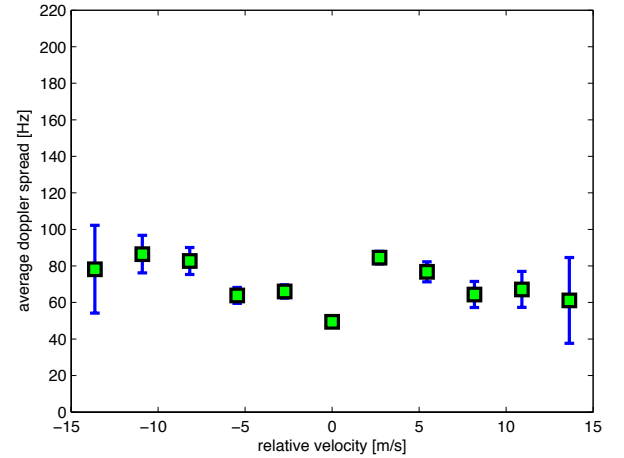
(a) Data set 2
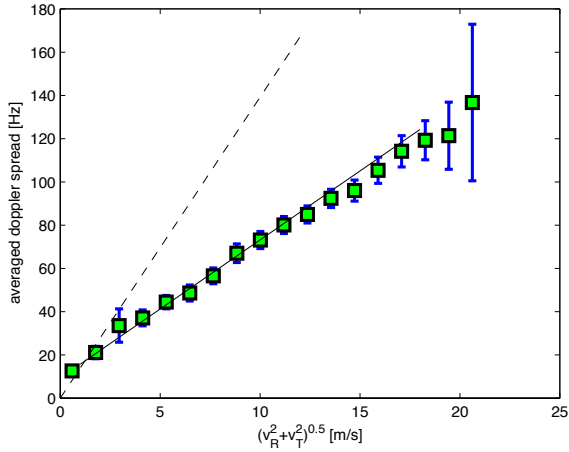
(b) Data set 2
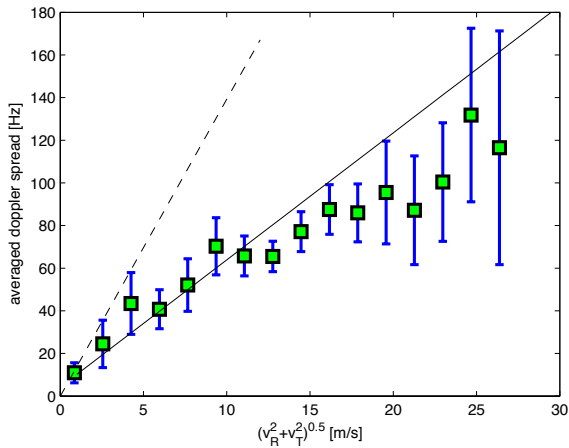
(c) Data set 1

Fig. 8. Doppler spread versus effective speed [26]. (a) contour plot of the Doppler spread from Data Set 2 versus v_T and v_R. (b) Doppler spread for Data Set 2 versus $v_{eff} = \sqrt{v_R^2(d) + v_T^2(d)}$. (c) Doppler spread for Data Set 1. The number of points in Data Set 1 was not sufficient for creating an accurate contour plot. The dashed line corresponds to Eq. 6, while the solid lines represent the linear regression given by Eq. 11.
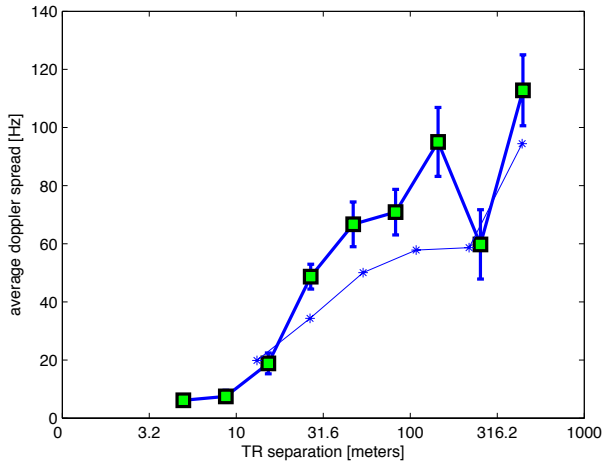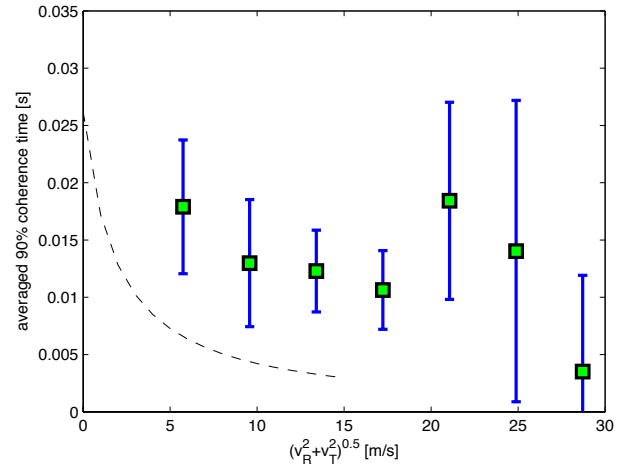

(a) Data set 1

(b) Data set 2

Fig. 9. Measured Doppler spread versus relative velocity for (a) Data set 1, and (b) Data set 2. All distances are included.

of Doppler spread calculated from the experimental spectra is good, demonstrating the validity and usefulness of the S-S diagram.

The S-S diagram allows others to compute the expected Doppler spectrum from just measurements of vehicle separation and speed. It should be noted that while an S-S diagram can be based on measurements, this is *not* required. In particular, it would be natural to simulate driver behavior in order to generate an S-S diagram and use that diagram to compute what the expected Doppler spread would be in such an environment. This would then allow the calculation of small-scale fading statistics and coherence time (as will be shown in the next section). This technique would be an extremely convenient way to generate accurate small-scale fading using only a model of driving behavior, with or without actual measurements.
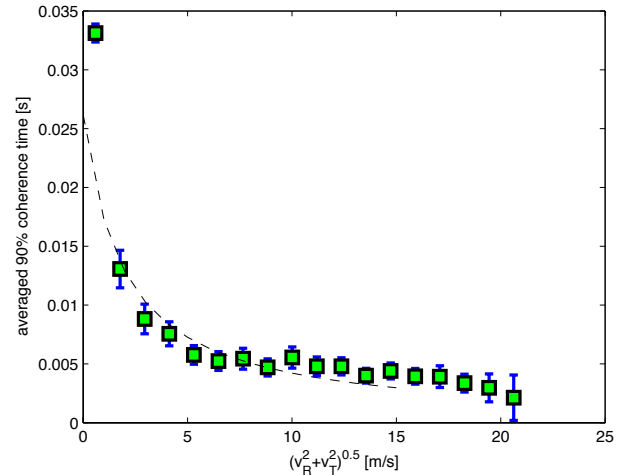
(a) Data set 1

(a) Data set 1
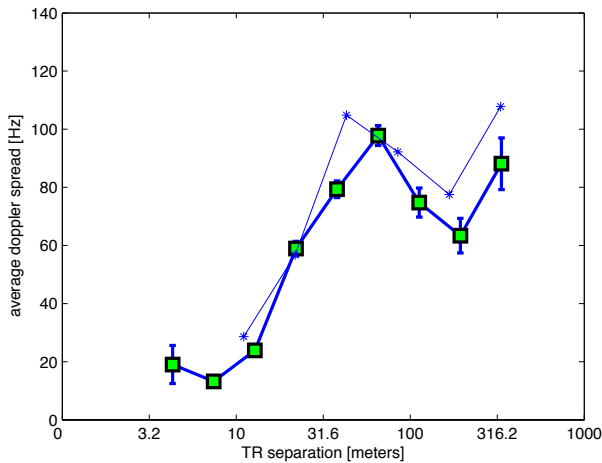
(b) Data set 2

(b) Data set 2

Fig. 10. Doppler spread versus Distance. (a) Data set 1, (b) Data set 2. Curves marked with "*" result from the S-S model.

Fig. 11. Coherence time versus relative velocity. (a) 90% coherence time for Data set 1, (b) 90% coherence time for Data set 2. Dashed lines superimposed are from $b\lambda/B_D$, where b is about 0.3.

VIII. COHERENCE TIME

Perhaps more directly related to the performance of digital communications systems is the coherence time, which represents the time interval over which the channel impulse response may be considered to be invariant. Although the coherence time and Dopper spread are inversely related [29], we compute the coherence time directly by evaluating the autocorrelation of the time-domain signal measured by the VSA. The 50% and 90% coherence times represent the time offsets for which the autocorrelation function drops to 50% or 90% of its peak value, respectively. Rather than directly computing the coherence time from the inverse of the Doppler spread, we compare the directly calculated Doppler spread to the directly calculated coherence time and compute a constant of proportionality that relates the two parameters.

The 90% coherence time values versus speed for both data sets are shown in Fig. 11. The dashed curves in the figure are proportional to the inverse Doppler spread as given by the linear regression in Fig. 8, $\tau_C = b/B_D$, where b is a constant of proportionality determined empirically. As can be seen, the value $b = 0.3$ gives reasonable agreement with the experimental 90% coherence time for Data Set 2. The agreement is not quite as good for Data Set 1 shown in Fig. 11(a), possibly due to the smaller size of the data set (larger error bars). It does appear, however, that the coherence time for Data Set 1 may somewhat longer than that for Data Set 2. And the b value agrees well with reported studies [25] [29].

As expected from the Doppler spread analysis, there is also a decrease in coherence time with distance for both data sets, as shown in Fig. 12. The experimental 50% and
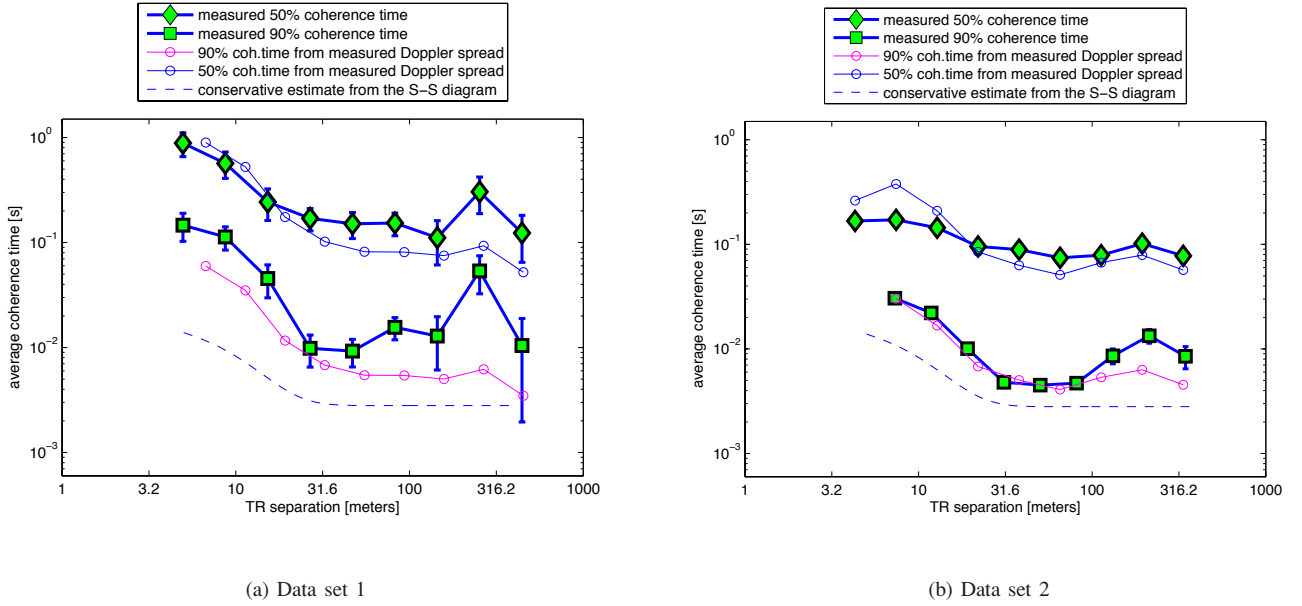
(a) Data set 1   (b) Data set 2

Fig. 12. Coherence time versus Distance. (a) Data set 1, (b) Data set 2. The solid line represents the estimates from the S-S diagram serving as a conservative bound.

90% coherence times are indicated by diamonds and squares, respectively. Also shown in Fig. 12 are the coherence times for each distance determined by the inverse of the experimental Doppler spread values from Fig. 10. These are seen to be in good agreement with the coherence times calculated directly from the time domain data.

It is important to note limitations in the accuracy of the coherence times shown in Fig. 12 owing to the finite duration of the VSA sweeps. The maximum 50% coherence time that can be measured is equal to the sweep duration, T_s, and the maximum 90% coherence time that can be measured is equal to $0.2T_s$ For Data Set 1, these limits are 1.5s and 0.3s for the 50% and 90% coherence times, respectively. For Data Set 2 the limits are 0.2s and 0.04s. The experimental values for Data Set 2 can be seen to approach these limits for distances below about 10 m, indicating that longer sweep durations are needed to accurately determine the coherence times at these close distances.

Finally, the inverse of the maximum Doppler shift from the phenomenological theory presented in Eq. 7 can be used to obtain a conservative estimate of the 90% coherence time using

$$\tau_C = \frac{b}{\left(\frac{0.428}{\lambda\sqrt{2}}\right) v_{eff,max} + 11.5}, \qquad (12)$$

where $v_{eff,max}$ is given by Eq. 7. This estimate is shown by the dashed lines in Fig. 12.

IX. SUMMARY AND CONCLUSIONS

We have described a measurement system to characterize V2V 5.9 GHz wireless communication channels. Measurements with this system provide insight into the propagation channel that we hope will facilitate the development and evaluation of DSRC technology. Our system features great

flexibility through the use of programmable signal generation and analysis to allow the use of arbitrary test signals up to 40 MHz in bandwidth. Our system also allows simultaneous channel measurements and DSRC prototype radio measurements. Lastly, the system is capable of making channel measurements as a function of location while the vehicles are in motion by integrating GPS receivers into our system, thereby allowing for larger, more varied measurement cases.

On-road experimental tests in a suburban area of Pittsburgh, Pennsylvania have characterized the V2V channel and validated the measurement platform we have created. These observations exceed the capabilities of measurements using only prototype DSRC radios and other systems. We also described in this paper narrowband sounding measurements, large-scale path loss models, fading models, coherence time, and doppler spread. In addition, we have developed insight into the impact of speed and separation distance on the Doppler spectrum. We have observed a correlation between speed and separation, and have interpreted this in terms of driver behavior. We have introduced the Speed-Separation (S-S) diagram as a new tool for understanding and predicting the properties of V2V wireless channels.

In particular, we have shown that the S-S diagram can be used to predict how Doppler spread and coherence time depend on the separation between the vehicles. The key concept behind the S-S diagram is recognition that the Doppler spread is proportional to effective speed. Consequently, a scatter plot of effective speed versus separation allows the estimation of Doppler spread (and hence coherence time) with separation. The boundaries of the data region on the S-S diagram can also be used to estimate maximum Doppler spreads and minimum coherence times with separation. This new tool provides a convenient way to accurately predict small-scale fading characteristics with or without actual measurements.

Although complete specification of the optimum signaling waveforms for the 5.9 GHz DSRC band requires wideband channel sounding in addition to the narrowband measurements presented here, our measurements do have important implications for wideband signals. For example, the maximum Doppler spread sets a lower limit on the carrier spacing used in OFDM transmissions and affects the fading statistics expected on each carrier, while the channel coherence time affects how long channel estimation is valid. For example, in DSRC packets, channel estimation is performed using a sequence of initial training symbols, and the results are applied to the entire packet. From our measurements, the 90% coherence time can be as small as 2-3 ms, suggesting that packets with durations longer than this may suffer higher error rates in a suburban environment.

Our work not only enables better comprehension of the V2V wireless channel with empirical data, but also serves as supplementary work to many theoretical modeling efforts on this topic. Present directions and future work include wide-band system analysis, theoretical channel modeling, and modulation scheme enhancement in DSRC.

Acknowledgment

Appendix: GPS Incorporation and Time Synchronization

One key feature of our measurement system is that location information can be retrieved from the GPS receiver, while the signal is recorded simultaneously. Such an enhanced system functionality enables us to analyze the location- and distance-based statistics. However, it introduces a technical challenge of synchronizing the transmitter side and the receiver side. In this appendix, we discuss a synchronization technique which could be used for synchronizing the clocks in different vehicles through the exchange of timestamps via data packet transmissions during the measurements. This technique is not used in this paper since it has been superseded by the use of GPS time information. We present it here though because it is of interest for synchronization in situations where GPS is not available, e.g., when using dead reckoning for position location.

A. Time Synchronization Requirement and NTP Protocol

A fundamental issue with V2V measurements is the necessity of synchronizing the data collected in two mobile yet separate vehicles. A key issue is how to align the data recorded on different computers with each other in terms of time. One technique is to utilize a variant of the Network Time Protocol (NTP) to match data collected from separate vehicles that were in motion.

The Network Time Protocol (NTP) is a commonly used method for synchronizing the clocks on different computers [20]. When NTP is used in a client/server mode, clients will first contact a server and request the current clock time.
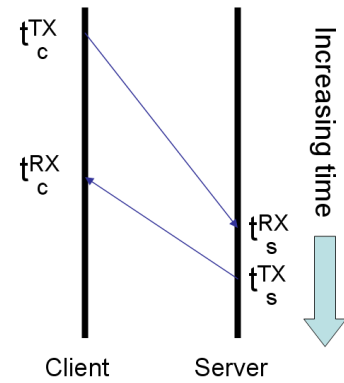
(a) Non-synchronized Clocks
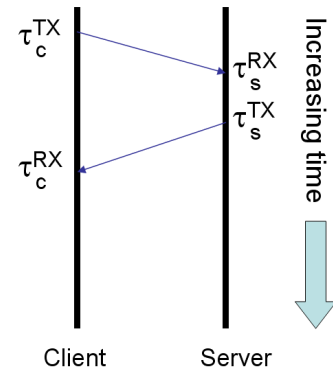
(b) Synchronized Clocks

Fig. 13. Packet exchange used by NTP to measure the clock offset between computers.

Then, the replied clock time from server computer is used to adjust the system clock at the client computer.

We do not recommend using the NTP protocol to synchronize the clocks of measurement computers in different vehicles. Instead we describe a modified algorithm similar to NTP. To better understand our algorithm we first briefly describe the calculation used by NTP to compute the clock offset between two computers. The top arrow in Fig. 13(a) represents the transmission of a packet from the client. The server replies with the current time in a packet transmitted to the client represented by the second arrow. The transmission and reception times for both packets are recorded and used to compute the offset in the clocks of the two computers. In the figure, the time stamps t_c^{TX}, t_c^{RX} represent the packet transmit and receive times, respectively, measured on the client clock, and t_s^{TX}, t_s^{RX} represent transmit and receive times on the server clock. Using the four time stamps, the clock offset T between the two cars is given by

$$T = \frac{\left(t_s^{RX} - t_c^{TX}\right) + \left(t_s^{TX} - t_c^{RX}\right)}{2}, \qquad (13)$$

which is given in [20]. Fig. 13(b) illustrates the packet exchange after using the time offset to synchronize the clocks. The time stamps shown in the figure are corrected using the formulas

$$\tau_c = t_c + T$$

$$\tau_s \;=\; t_s.$$

Thus by using the measured propagation delay, the correct system time can be set by the client computer.

B. Alternative Time Synchronization Technique

In our measurement setup, prototype DSRC radios are used to exchange GPS location and other useful information between vehicles. A natural idea for time synchronization would be to simply use NTP over this link. However, wireless links have bursty and asymmetric delays that could cause errors in the NTP based synchronization. To ensure the fidelity of the measurement data, the synchronization of clocks on the different measurement computers should not be significantly affected by spontaneous wireless link errors in an uncorrectable fashion. For this reason, we describe an NTP-like post-processing technique that allows clock synchronization to occur without being affected by wireless link errors. In other words, synchronization of clocks is still achieved even though wireless links occasionally fail.

The technique synchronizes two remote computers by transmitting packets from one vehicle to the other vehicle at a regular rate. Transmission and reception timestamps are recorded in the same manner as done by NTP shown in Fig. 14. However, the clocks of the vehicles should not be adjusted during the measurement. Instead, a clock offset between the vehicles is computed in a post-processing procedure after the completion of the empirical measurement campaign. To do this, we adapt Eqn.13 using all of the packet transmission time stamps collected in the measurement. Assuming an equal number of packets, N, are exchanged in both directions, we compute the new clock offset T' as

$$
\begin{aligned}
T' &= \frac{1}{N}\sum_{i=1}^{N}\sum_{j=1}^{N}\frac{\left(t_{b,i}^{RX}-t_{a,i}^{TX}\right)+\left(t_{b,j}^{TX}-t_{a,j}^{RX}\right)}{2}\\
&= \frac{1}{2N}\left(\sum_{i=i}^{N}(t_{b,i}^{RX}-t_{a,i}^{TX})+\sum_{j=1}^{N}(t_{b,j}^{TX}-t_{a,j}^{RX})\right)
\end{aligned}
\tag{14}
$$

This equation can be further modified for the case where a different number of packet transmissions take place from vehicle a to vehicle b, N_{ba}, than their counterparts take place from vehicle b to vehicle a, N_{ab}. The extended equation is given as

$$
T' = \frac{1}{2}\left(\frac{1}{N_{ba}}\sum_{i=1}^{N_{ba}}\left(t_{b,i}^{RX}-t_{a,i}^{TX}\right)+\frac{1}{N_{ab}}\sum_{j=1}^{N_{ab}}\left(t_{b,j}^{TX}-t_{a,j}^{RX}\right)\right).
\tag{15}
$$

Clock drift is not a significant concern in short measurement runs lasting for up to about an hour. However, the system clocks of multiple computers located at disconnected vehicle nodes may drift with respect to one another over the course of a long measurement campaign. One way to compensate for this is by computing T' over hour long intervals throughout the measurement run to correct for clock drift.
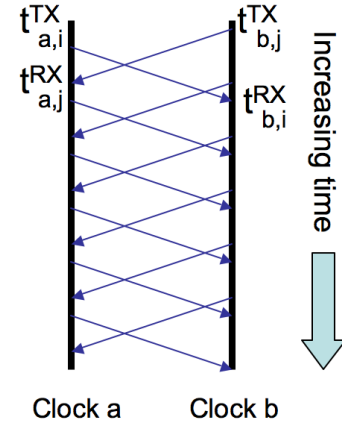

Fig. 14. Illustration of packets exchanged between vehicles and the timestamps recorded.

REFERENCES

[1] Jing Zhu and Sumit Roy, "Mac for dedicated short range communications in intelligent transport system," *IEEE Communications Magazine*, pp. 60–67, 2003.
[2] Jijun Yin, Tamer ElBatt, Gavin Yeung, Bo Ryu, Stephen Habermas, Hariharan Krishnan, and Timothy Talty, "Performance evaluation of safety applications over DSRC vehicular ad hoc networks," *VANET '04: Proceedings of the 1st ACM international workshop on Vehicularad hoc networks*, pp. 1–9, 2004.
[3] Jeremy J. Blum, Azim Eskandarian, and Lance J. Hoffman, "Challenges of intervehicle ad hoc networks," *IEEE Trans. on Intelligent Transportation Systems*, vol. 5, pp. 347–351, 2004.
[4] F. Haber A. S. Akki, "A statistical model of mobile-to-mobile land communication channel," *IEEE Trans. on Vehicle Technology*, vol. VT-35, 1986.
[5] A. S. Akki, "The influence of mobile-to-mobile land communication channel spectrum on the error rate of binary dpsk and nfsk matched filter receivers," *IEEE Trans. on Vehicle Technology*, vol. 43, pp. 832 – 836, 1994.
[6] A. S. Akki, "Statistical properties of mobile-to-mobile land communication channels," *IEEE Trans. on Vehicle Technology*, vol. 43, pp. 826 – 831, 1994.
[7] R. Wang and D. Cox, "Double mobility mitigates fading in ad hoc wireless networks," *IEEE Antennas and Propagation Society International Symposium*, vol. 2, pp. 16–21, 2002.
[8] R. Wang and D. Cox, "Channel modeling for ad hoc mobile wireless networks," *IEEE Vehicular Technology Conference*, pp. 21 – 25, 2002.
[9] Chirag Patel, Gordon Stuber, and Thomas G. Pratt, "Simulation of rayleigh-faded mobile-to-mobile communication channels," *IEEE Transactions on Communications*, pp. 1876 – 1884, 2005.
[10] Li-Chun Wang and Yun-Huai Cheng, "A statistical mobile-to-mobile rician fading channel model," *Vehicular Technology Conference, VTC 2005-Spring, IEEE 61st*.
[11] J.S. Davis and J.P.M.G. Linnartz, "Vehicle to vehicle RF propagation measurements," *Twenty-Eighth Asilomar Conference on Signals, Systems and Computers*, vol. 1, pp. 470 – 474, 1994.
[12] Ratish J. Punnoose, Pavel V. Nikitin, Josh Broch, and Daniel D. Stancil "Optimizing Wireless Network Protocols Using Real-Time Predictive Propagation Modeling" *Radio and Wireless Conference (RAWCON)*, 1999.
[13] Guillermo Acosta, Kathleen Tokuda, and Mary Ann Ingram, "Measured joint doppler-delay power profiles for vehicle-to-vehicle communications at 2.4 GHz," *GLOBECOM '04. IEEE*, vol. 6, pp. 3813 – 3817, 2004.
[14] J. Maurer, T. Fugen, and W. Wiesbeck, "Narrow-band measurements and analysis of the inter-vehicle transmission channel at 5.2 ghz," *Vehicular Technology Conference, 2002. VTC Spring 2002. IEEE 55th*, vol. 3, pp. 1274 – 1278, 2002.
[15] Xiongwen Zhao, Jarmo Kivinen, Pertti Vainikainen, and Kari Skog, "Characterization of Doppler spectra for mobile communications at 5.3 GHz," *IEEE Transactions on Vehicular Technology*, vol. 52, pp. 14–23, 2003.
[16] Xiongwen Zhao, Jarmo Kivinen, Pertti Vainikainen, and Kari Skog, "Propagation characteristics for wideband outdoor mobile communica-

tions at 5.3 ghz," *IEEE Journal on Selected Areas in Communications*, vol. 20, no. 3, pp. 507–514, April 2002.

[17] Guillermo Acosta and Mary Ann Ingram, "Doubly Selective Vehicle-to-Vehicle Channel Measurements and Modeling at 5.9 GHz," *Proceedings 2006 Wireless Personal Multimedia Communications Conference (WPMC'06)*, September 17-20, 2006.

[18] Denso Corporation North America Lab, "Technical Specification of Dedicated Short-Range Communication (DSRC) Radio" *Denso Corporation*, 2004.

[19] Lin Cheng, Benjamin Henty, Daniel Stancil, Fan Bai and Priyantha Mudalige, "Fully Mobile, GPS Enabled, Vehicle-to-Vehicle Measurement Platform for Characterization of the 5.9 GHz DSRC Channel," *IEEE International Symposium on Antennas and Propagation*, June, 2007.

[20] David. L. Mills, "Network Time Protocol (Version 3) Specification, Implementation and Analysis," Internet Engineering Task Force, *Request for Comments: RFC-1305, Network Working Group*, Mar. 1992.

[21] W. Gellert, S. Gottwald, M. Hellwich, H. Kastner, and H. Kustner, "The VNR Concise Encyclopedia of Mathematics" *2nd ed. ch. 12*, Van Nostrand Reinhold: New York, 1989.

[22] U.S. Census Bureau Geographical Systems FAQ, "Q5.1: What is the best way to calculate the distance between 2 points?" http://www.census.gov/cgi-bin/geo/gisfaq?Q5.1, 2001.

[23] H. Masui, T. Kobayashi and M. Akaike "Microwave path-loss modeling in urban line-of-sight environments" *IEEE Journal on Communications*, Volume 20, Issue 6, Aug. 2002 Page(s):1151 - 1155.

[24] Fan Bai, Narayanan Sadagopan, Bhaskar Krishnamachari, and Ahmed Helmy, "Modeling Path Duration Distributions in MANETs and Their Impact on Reactive Routing Protocols" *IEEE Journal on Selected Areas of Communications*, Vol. 22, No. 7, Sep. 2004.

[25] J. D. Parsons, "The Mobile Radio Propagation Channel" *2nd ed*., John Wiley and Sons, 2000.

[26] Lin Cheng, Benjamin Henty, Daniel Stancil, Fan Bai and Priyantha Mudalige, "Properties and Applications of the Suburban Vehicle-to-Vehicle Propagation Channel at 5.9 GHz (Invited paper)," *International Conference on Electromagnetics in Advanced Applications*, Sept, 2007.

[27] M. D. Shupe, S. Y. Matrosov, T. L. Schneider and P. Kollias "Mixed-Phase Cloud Retrievals Using Doppler Radar Spectra" *Thirteenth ARM Science Team Meeting Proceedings*, 2003.

[28] M. D. Shupe, P. Kollias, S. Y. Matrosov and T. L. Schneider, "Mixed-Phase Cloud Retrievals Using Doppler Radar Spectra" *Journal of atmosphere and oceanic technology*, Volume 21, 2004 Page(s):660 - 670.

[29] Bernard Sklar, "Rayleigh Fading Channels in Mobile Digital Communication Systems Part 11: Mitigation" *IEEE Communications Magazine*, July 1997, pp. 102-109.

He has also studied time-reversal focusing and was one of the first to demonstrate multipath enabled super-resolution spatial focusing possible at RF frequencies. In addition to his research interests in V2V networks, he has also helped to demonstrate inverse Doppler shift phenomena in magnetic spin waves. Benjamin has also worked in small startup companies designing electromagnetic propagation prediction software and indoor cellular and wireless LAN networks.

Daniel D. Stancil (S'75-M'81-SM'91-F'03) received the B.S. degree in Electrical Engineering from Tennessee Technological University, Cookeville, in 1976, and the S.M., E.E. and Ph.D. degrees from the Massachusetts Institute of Technology, Cambridge, in 1978, 1979, and 1981, respectively.

From 1981 to 1986 he was Assistant Professor of Electrical and Computer Engineering at North Carolina State University, Raleigh. He joined the faculty at Carnegie Mellon University in 1986 as an Associate Professor, since becoming Professor. From 1992-1994 he served as Associate Department Head of the Department of Electrical and Computer Engineering, and served as Associate Dean for Academic Affairs in the College of Engineering from 1996-2000. In 1996 he co-founded the Applied Electro-optics Corporation. His research interests include wireless communications and optical data storage.

Dr. Stancil received a Sigma Xi Research Award from North Carolina State University in 1985, and was a leader in the development of the CMU ECE department's Virtual Laboratory which was a finalist for a 1996 Smithsonian Computerworld Award. In 1998 he was corecipient of a Science Award for Excellence from the Pittsburgh Carnegie Science Center, a Research and Development 100 Award, and a Photonics Circle of Excellence Award for the development and commercialization of electrooptic technology.

Lin Cheng received the B.S. degree from Shanghai Jiaotong University, Shanghai, China, and the M.Sc. degree from Carnegie Mellon University, Pittsburgh, PA. He is currently working toward the Ph.D. degree in the Department of Electrical and Computer Engineering, Carnegie Mellon University. His industrial experience includes periods with Intel and Siemens Corporate Research.

His research interest includes wireless communications, propagation modeling, and RF systems. He is also interested in medical image processing and computer vision, with a focus on image reconstruction and segmentation especially for low-dose imaging. His current research is focused on design principles for the next-generation Vehicular Ad hoc Networks (VANET).

Benjamin E. Henty is recent doctoral graduate of Carnegie Mellon University in Electrical and Computer Engineering. He received a MSEE at Virginia Tech University and a BSECE degree from Carnegie Mellon as well.

For his doctoral research, Benjamin focused on utilizing building ventilation ducts to improve wireless communications indoors. He deployed the first full building installation of IEEE 802.11g access points in Stavanger, Norway using a ventilation duct antenna system (VDAS) and is aiding in the commercialization of the technology.

Fan Bai is a Senior Researcher in the Electrical and Control Integration Lab., Research and Development Center, General Motors Corporation. Before joining General Motors research lab, he received the B.S. degree in automation engineering from Tsinghua University, Beijing, China, in 1999, and the M.S.E.E. and Ph.D. degrees in electrical engineering, from University of Southern California, Los Angeles, California, U.S.A., in 2005.

His current research is focused on the discovery of fundamental principles and the analysis and design of protocols/systems for next-generation Vehicular Ad hoc Networks(VANET). Dr. Bai has published about 30 conference and journal papers, including INFOCOM, MobiHoc, SECON, IEEE JSAC, IEEE Wireless Communication Magazine and Elsevier AdHoc Networks Journal. He received the Charles L. McCuen Special Achievement Award from General Motors Corporation for his research contributions to VANET field in 2006. He also serves as the Technical Program Co-Chair of 1st IEEE International Symposium on Wireless Vehicular Communications (IEEE WiVec 2007).

Priyantha Mudalige is an IEEE member and a chartered professional engineer with eighteen years of industry experience. Currently, he is a senior researcher at General Motors R&D, Warren, Michigan. His research interests are vehicle-to-vehicle communication based active safety systems, autonomous vehicles, collision avoidance, vision, and embedded software development. Priyantha holds B.Sc Eng (Honors) degree from University of Moratuwa, Sri Lanka in 1987 and M.S. Engineering degree from University of New South Wales, Australia in 1993.